RSC Advances

PAPER

View Article Online
View Journal | View Issue

Cite this: *RSC Adv.*, 2025, **15**, 34635

Synthesis, characterization, DNA interaction, and anticancer studies of novel *facial* tricarbonylrhenium(I) complexes with uracil-derived ligands

Shabaaz Abdullah,[a] Candace Davison,[b] Christie Jane Smit,[b] Phiwokuhle Mbatha,[a] Jo-Anne de la Mare*[b] and Irvin Noel Booysen *[a]

Herein, we report the formation and characterisation of novel rhenium(I) complexes with bidentate uracil chelating ligands. Three metal complexes including *fac*-[Re(CO)$_3$(urda)Cl] (**1**) (urda = 5, 6-diamino-1, 3-dimethyluracil), *fac*-[Re(CO)$_3$(uramb)Br] (**2**) (uramb = amino-5-((2-aminobenzylidene)amino)-1,3-dimethyluracil) and *fac*-[Re(CO)$_3$(urqn)Br] (**3**) (urqn = amino-5-((isoquinolin-3-ylmethylene)amino)-1,3-dimethyluracil) were spectroscopically characterized. Structural elucidations were corroborated by single-crystal X-ray crystallography, TOF mass spectrometry, and elemental analysis. These metal complexes retain their structural integrity in aqueous media during UV-Vis spectrophotometric titrations. Anticancer screening of the metal complexes was done in two cancer cell lines, HCC70 and HeLa, as well as in a benign MCF12A cell line. In particular, while complex **1** was highly cytotoxic towards HeLa cells and was non-toxic to HCC70 TNBC and MCF12A non-cancerous cells, complex **2** displayed low micromolar toxicity in all three cell lines and was selected for further analysis. This metal complex exhibits dual DNA intercalation and groove-binding modes, however this did not lead to DNA damage as assessed by a comet assay. In addition, metal complex **2** did not appear to inhibit topoisomerase activity, suggesting a different mechanism of action from that reported for ruthenium complexes with topoisomerase inhibitory activities.

Received 25th July 2025
Accepted 11th September 2025

DOI: 10.1039/d5ra05387k

rsc.li/rsc-advances

Introduction

The use of the *facial* tricarbonylrhenium core in the development of functional therapeutic radiopharmaceuticals is an ongoing venture since this robust metal core portrays numerous favourable properties.[1–4] In particular, coordination complexes of rhenium(I) are typically kinetically and thermodynamically stable owing to the metal centre's low-spin d^6 electron configuration. In addition, the optimal hydrophilicity offered by the co-ligands of the *fac*-[Re(CO)$_3$]$^+$ moiety can render aqueous miscibility and stability. Furthermore, meticulous considerations of the organic chelators' donor atoms and structural features can facilitate cellular uptake and target-specificity.[5,6]

Schiff bases derived from 5, 6-diamino-1, 3-dimethyluracil (urda) have shown characteristic coordination behaviours towards the *fac*-[Re(CO)$_3$]$^+$ and [Re^{V}O]$^{3+}$ cores.[7,8] Of particular interest is the model rhenium(I) complex, *fac*-[Re(CO)$_3$(urpy)Br] (urpy = amino-1,3-dimethyl-6-((pyridin-2-ylmethylene)amino) uracil), where the neutral bidentate Schiff base chelator forms a five-membered chelate ring through its $N_{\text{imino}}N_{\text{pyridyl}}$ donor set. Consequently, the uracil pharmacophore remains uncoordinated, which, as per the design strategy, may promote a defined biodistribution pattern and strong binding with the cancerous target site. In fact, 5-substituted uracil complexes such as uracil mustard and fluorouracil are widely used as chemotherapeutic agents.[9]

Considering the favourable structural features of the model complex, the objective was to form and characterise new *facial* tricarbonylrhenium(I) complexes with bidentate uracil Schiff base chelators. Therefore, the rhenium(I) complex, *fac*-[Re(CO)$_3$XBr] [X = amino-5-((2-aminobenzylidene)amino)-1,3-dimethyluracil (uramb) for **2**, and amino-5-((isoquinolin-3-ylmethylene)amino)-1,3-dimethyluracil (urqn) for **3**] were isolated, see Fig. 1. In addition, the rhenium complex, *fac*-[Re(CO)$_3$(urda)Cl] (**1**), containing a coordinated urda ligand, afforded an interesting structure–activity relationship when compared to **2** and **3**. Biomolecular interaction studies were performed to delineate the mechanism of anticancer activity of the most cytotoxic metal compound.

[a]*School of Chemistry and Physics, University of KwaZulu-Natal, Pietermaritzburg, 3201, South Africa. E-mail: booyseni@ukzn.ac.za*

[b]*Department of Biochemistry, Microbiology and Bioinformatics, Faculty of Science, Rhodes University, PO Box 94, Grahamstown 6140, South Africa. E-mail: j.delamare@ru.ac.za*

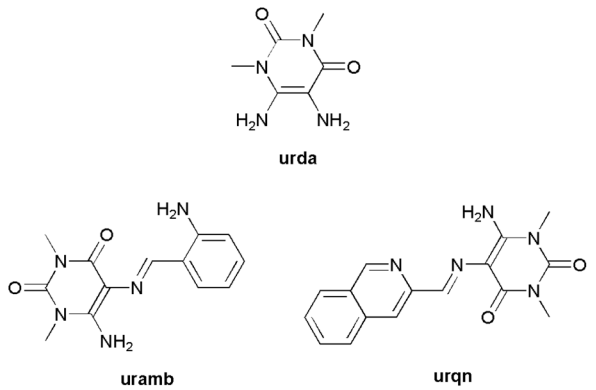

Fig. 1 Structure of the organic scaffold 5, 6-diamino-1, 3-dimethyluracil (urda) as well as the uracil Schiff base structures: amino-5-((2-aminobenzylidene)amino)-1,3-dimethyluracil (uramb) and amino-5-((isoquinolin-3-ylmethylene)amino)-1,3-dimethyluracil (urqn), which were used during this study.

Experimental

Materials and methods

All chemicals were obtained from Sigma-Aldrich, and these chemicals are listed within the accompanying online SI document. The urpy and uramb Schiff bases were synthesised according to previously published methods.[7,8] The SI also describes the details of the instrumentation used for structural elucidations of the novel free-ligand and the metal complexes.

Synthesis of 6-amino-1,3-dimethyl-5-((uinoline-2-ylmethylene)amino)pyrimidine-2,4-(1*H*, 3H)-dione (urqn).

Urda (1.00 g; 5.88 mmol) was condensed with 2-quinolinecarboxaldehyde (0.92 g; 5.88 mmol) in hot ethanol (30 cm^3) for 3 hours under reflux conditions. Afterwards, a yellow precipitate was claimed *via* vacuum filtration and washed with cold methanol, diethyl ether and petroleum ether. Thereafter, a yellow crystalline precipitate was obtained from hot recrystallisation in ethanol. Yield = 70%; melting point: 271.0–274.2 °C; infrared (ν_{max}/cm^{-1}): ν(N–H)$_{stretch}$ 3107 (br), ν(C=O) 1685, 1593 (s), ν(C=N) 1497 (s), ν(C–N) 1060 (s), ν(N–H)$_{bend}$ 742 (s), ^{1}H NMR (303 K ppm^{-1}): 9.87 (s, 1H, H4), 8.61 (d, 1H, H10), 8.31 (d, 1H, H5), 8.01–7.95 (dd, 2H, H6, H9), 7.75–7.72 (t, 1H, H5), 7.59–7.55 (t, 3H, H3, H8), 3.43 (s, 3H, H2), 3.20 (s, 3H, H1), see Fig. S1; ^{13}C NMR (303 K ppm^{-1}): 157.97, 157.67, 154.66, 150.23, 149.88, 148.00, 136.17, 130.00, 129.31, 128.28, 128.25, 127.01, 118.68, 99.62, 30.94, 27.64, see Fig. S2; UV-Vis (DMF, λ_{max} (ε, M^{-1} cm^{-1})): 385 nm (76 250), 282 nm (46 870); molecular mass (*m*/*z*): calcd: 309.32, found: 308 [M–H]$^-$, 371 [M–H + 2MeOH]$^-$, see Fig. S3; anal. calc. for $C_{16}H_{15}N_5O_2$: C, 62.13; H, 4.89; N, 22.64; found: C, 62.38; H, 4.55; N, 22.76%.

Synthesis of *fac*-[Re(CO)$_3$(urda)Cl] (1)

The titled metal complex was synthesised by reacting urda (0.0941 g, 0.553 mmol) and [Re(CO)$_5$Cl] (0.2000 g, 0.553 mmol) in anhydrous toluene (30 cm^3) under an inert atmosphere. The reaction mixture was heated under reflux for 6 hours, resulting in the formation of a purple precipitate. This precipitate was filtered and washed with methanol, diethyl ether and petroleum ether. Yellow, irregularly shaped cuboid crystals were obtained *via* vapour diffusion of hexane into tetrahydrofuran. Yield: 53%; melting point: 268.5–282.3 °C. Infrared (ν_{max}/cm^{-1}): ν(N–H)$_{stretch}$ 3213 (br, m), ν(C≡O)$_{fac}$ 2020, 1888 (s), ν(C=O) 1713 (s), ν(C=N) 1606 (s), ν(C–N) 1519 (*vs.*), 1245 (s), ν(N–H)$_{bend}$ 747 (s); ^{1}H NMR (303 K ppm^{-1}): 7.59 (s, 2H, N_5H_2), 6.51 (d, 1H, N10H), 4.86 (d, 1H, N10H′), 3.34 (s, 3H, C10H$_3$), 3.21 (s, 3H, C6H3); ^{13}C NMR (303 K ppm^{-1}): 197.86, 197.59, 192.91, 168.62, 153.63, 149.08, 90.91, 30.63, 28.47, see Fig. S4; UV-Vis (DMF, λ_{max} (ε, M^{-1} cm^{-1})): 365 nm (456), 488 nm (310); molecular mass (*m*/*z*): calcd: 475.86, found: 475 [M]$^-$, 439 [M–Cl]$^-$; anal. calc. for $C_9H_{10}ClN_4O_5Re$: C, 22.72; H, 2.12; N, 11.77; found: C, 23.12; H, 2.03; N, 11.81%.

Synthesis of *fac*-[Re(CO)$_3$(uramb)Br] (2)

A reaction mixture of [ReCO$_5$Br] (0.104 g; 0.256 mmol) and uramb (0.07 g; 0.256 mmol) was stirred in 30 cm^3 anhydrous toluene and left to reflux at 100 °C for 6 hours. During the aforementioned reaction, a pale-yellow precipitate formed, which was filtered and washed with cold methanol, diethyl ether and petroleum ether. Yellow needle-like crystals were obtained *via* vapour diffusion of hexane into tetrahydrofuran, and these were suitable for single-crystal X-ray diffraction. Yield: 44%; melting point: 271.0–274.2 °C. Infrared (ν_{max}/cm^{-1}): ν(C–H) 3383, 3312 (s), ν(N–H)$_{stretch}$ 3200, 3045 (br, m), ν(C≡O)$_{fac}$ 2024 (s), 1900 (*vs.*), ν(C=O) 1662 (s), ν(C=N) 1638 (s), ν(C–N) 1474 (s), 1206 (s), ν(N–H)$_{bend}$ 747 (s); ^{1}H NMR (303 K ppm^{-1}): 8.31 (s, 1H, H8), 7.73–7.70 (d, 1H, N_2H), 7.60–7.56 (t, 1H, H17), 7.52–7.51 (d, 1H, H18), 7.39–7.31 (m, 2H, H15, H16), 6.60 (s, 2H, N6H$_2$), 6.46–6.43 (d, 1H, N2H′), 3.45 (s, 3H, C10H$_3$), 3.31 (s, 3H, C13H3); ^{13}C NMR (303 K ppm^{-1}): 194.16, 178.51, 151.30, 147.52, 141.69, 136.28, 134.97, 130.51, 128.34, 126.87, 116.75, 116.04, 112.98, 29.85, 28.36, see Fig. S5; UV-Vis (DMF, λ_{max} (ε, M^{-1} cm^{-1})): 297 nm (46 308), 367 nm (23 382), 441 nm (14 697); molecular mass (*m*/*z*): calcd: 623.43, found: 622 [M–H]$^-$; anal. calc. for $C_{20}H_{23}BrN_5O_6Re$: C, 34.54; H, 3.33; N, 10.07; found: C, 34.42; H, 2.68; N, 9.94%.

Synthesis of *fac*-[Re(CO)$_3$(urqn)Br] (3)

A 1 : 1 molar coordination reaction between urqn (0.1523 g, 0.492 mmol) and [Re(CO)$_5$Br] (0.2000 g, 0.492 mmol) by refluxing the resultant solution for 6 hours in dry toluene (30 cm^3) at 100 °C under an inert atmosphere. Subsequently, a red precipitate was filtered and washed with cold methanol, diethyl ether and petroleum ether. Red cubic crystals were obtained *via* slow diffusion of hexane into dichloromethane. Yield: 64%; melting point: 290.8–293.9 °C. Infrared (ν_{max}/cm^{-1}): ν(N–H)$_{stretch}$ 3209 (br, m), ν(C≡O)$_{fac}$ 2020 (s), 1890 (*vs.*), ν(C=O) 1692 (s), ν(C=N) 1610 (*vs.*), ν(C–N) 1500 (s), 1442 (s), 1057 (s), ν(N–H)$_{bend}$ 753(s); ^{1}H NMR (303 K ppm^{-1}): 9.61 (s, 1H, H4), 9.00 (d, 1H, H16), 8.70 (t, 1H, H17), 8.45 (d, 1H, H12), 8.32 (d, 1H, H13), 8.20–8.16 (t, 1H, H18), 7.99–7.95 (t, 1H, H19), 7.49 (d, 2H, N6H$_2$), 3.43 (s, 3H, C9H$_3$), 3.26 (s, 3H, C7H$_3$); ^{13}C NMR (303 K ppm^{-1}): 196.90, 195.16, 185.99, 177.04, 156.56, 155.52, 149.62, 148.53, 146.86, 141.82, 133.49, 130.01, 129.70, 128.79, 124.72,

106.94, 30.18, 28.17, see Fig. S6; UV-Vis (DMF, λ_{max} (ε, M^{-1} cm^{-1})): 336 nm (21 620), 455 nm (18 740); molecular mass (*m*/*z*): calcd: 659.46, found: 658 $[M-H]^-$; anal. calc. for $C_{19}H_{15}BrN_5O_5Re$: C, 34.60; H, 2.29; N, 10.62; found: C, 34.75; H, 2.09; N, 10.39%.

Biological and computational studies

The experimental methods employed for the *in vitro* anticancer, DNA binding, Topoisomerase I inhibition and Alkaline Comet assay studies are similar to those reported previously.[10] Similarly, computational studies were performed in a comparable manner to other rhenium(I) compounds. Please refer to the SI document for the detailed experimental methods of the biological and computational studies.

Results and discussion

Synthesis and spectral characterisation

The new uracil-derived Schiff base, uramb was formed from the equimolar condensation reaction of urda with the respective 2-substituted aromatic aldehyde, 2-aminobenzaldehyde. The recrystallised Schiff base was isolated in a high yield and is readily soluble in chlorinated and aprotic solvents at ambient temperatures, while the solubility gradually increases in low molecular weight alcohols. Furthermore, all three monomeric complexes were formed from 1 : 1 coordination reactions of $[Re(CO)_5X]$ (X = Cl for **1**, Br for **2** and **3**) with the free ligands: urda, uramb and urqn, respectively.

Indicative of the model rhenium(I) complex, *fac*-$[Re(CO)_3$(-urpy)Br], the uracil Schiff base chelators of **2** and **3** act as neutral bidentate chelators but have different donor sets, *viz.* N_{imino}-N_{amino} for **2** and $N_{imino}N_{quinoline}$ for **3**. However, the urda chelator of **1** coordinates *via* its uracil ketonic oxygen and an amino nitrogen, which is indicative of a reported mononuclear complex, *fac*-$[ReCl(CO)_3$(DANU)] (DANU = 6-amino-1,3-dimethyl-5-nitroso-2,4-(1*H*, 3*H*)-uracil) that has the same donor set of **1**.[11] Despite the fact that the metal complexes were recrystallised in the same manner, low conversion yields were attained for **1** and **2**, whereas **3** was isolated in moderate to high yields. In addition, the metal complexes are soluble in polar organic solvents such as methanol, ethanol, dichloromethane, acetonitrile and tetrahydrofuran.

Generally, the ^{1}H NMR signals of **2** and **3** shift downfield relative to the analogous signals of their corresponding free-ligands, which emphasises the differences in the chemical environments between the former and the latter, see Fig. S7 and S8. In fact, the protons of the coordinated amino nitrogen are split in the NMR spectrum of **1**, and these signals resonate as doublets at 6.51 and 4.86 ppm, see Fig. S9. It is apparent that the electronic properties of the chelators' Schiff base functionalities are altered upon coordination to the *fac*-$[Re(CO)_3]^+$ core since the imino singlets of the coordinated and free Schiff bases differ. A similar spectral trend is observed in **3**, when comparing the imino signal of the metal complex (at 9.61 ppm) and its corresponding free-ligand (at 9.87 ppm). Also, in the case of **2**, a substantial downfield shift in the imino proton singlet (at 8.31 ppm) is observed with respect to the related signal of the uncoordinated Schiff base (at 9.65 ppm).

A fingerprint feature of the infrared spectra of the rhenium(I) complex are narrow [2020 cm^{-1} for **1** 2024 cm^{-1} for **2** and 2020 cm^{-1} for **3**] and broad [1888 cm^{-1} for **1**, 1900 cm^{-1} for **2** and 1890 cm^{-1} for **3**] intense vibrations of their carbonyl co-ligands which are arranged in *facial* orientations around their respective central metal centres, see Fig. S10–S12.[12] Infrared vibrations associated with the amine stretching and bending modes occur as medium-intensity and broad bands in the following regions: 3187–3213 cm^{-1} [for $\nu(N-H)_{stretch}$] and 747–755 cm^{-1} [for $\nu(N-H)_{bend}$]. Strong Schiff base ν(C=N) vibrations of the metal complexes **2** and **3** appear at 1638 and 1610 cm^{-1}, which are comparable to other signals of the Schiff base rhenium(I) complex that occurs in the range of 1562–1643 cm^{-1}.[8,13,14] Of particular interest is that more energy is required to vibrate the uracil ketonic bond of **1** vibrates (at 1713 cm^{-1}) oppose to the analogous ν(C=O) signals of the that's attributed to the metal centre of **1** coordinating directly to its urda moiety, see Fig. S10.

The electronic spectra of the mononuclear metal complexes illustrate alterations in their pi–pi* intra-ligand transitions (<380 nm) compared to those of the free Schiff bases. In turn, the aforementioned spectral trend rationalises the variations in the NMR signals of the chelator and free-Schiff base pairs. This is further emphasised by charge transfers occurring from the metal centres to their individual donor sets, and these MLCT bands are found at 488 nm for **1**, at 441 nm for **2** and at 455 nm for **3**, see Fig. S13–S15.[15] Metal-based d–d transitions aren't apparent due to the low-spin d^6 electron configurations of their central metal atoms.[13]

In the mass spectra of metal complexes **1–3**, the molecular ion peaks appear in the SI-negative mode, see Fig. S16–S18. Two significant peaks were present in the MS spectrum of complex **1**, which were assigned M–Cl]$^-$ (at *m*/*z* 439) and $[M]^-$ (at *m*/*z* 475). Mass spectrometric analyses of **2** and **3** reveal molecular ion peaks corresponding to a loss of a proton for each species. Their elemental analysis data indicated that the metal complexes are pure since the differences between the theoretical and experimental CHN elemental compositions are below 0.5%. In the case of **2**, the rigorous drying of its crystalline material in a vacuum oven led to the removal of one THF solvent molecule from the crystal lattice.

Crystallographic description

Complex **1** co-crystallised out with a tetrahydrofuran molecule of recrystallisation in a *P*-1 space group, where two crystallographically-independent molecules of each occupy their asymmetric unit cell, see Fig. 2 and Table S1. Similarly, complex **2** crystallises out in a *P*-1 space group, but its orthorhombic crystal system affords an 8 : 8 ratio comprised of its molecules and tetrahydrofuran molecules of recrystallisation, see Fig. 3. The molecules of **3** adopt a $P2_1/c$ space group, where the monoclinic unit cells occupy four molecules, see Fig. 3.

Extensive intermolecular interactions occurring between adjacent molecules of **1** and their neighbouring solvent

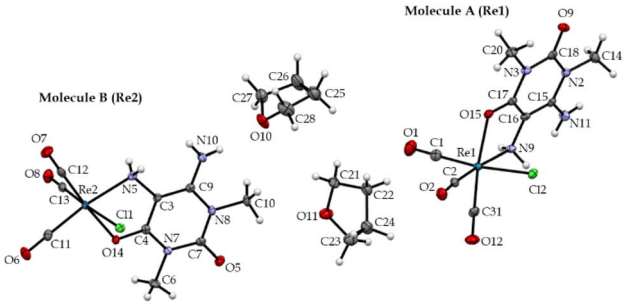

Fig. 2 A solid-state structure showing the two crystallographically-independent molecules of **1** along with their solvent molecules of recrystallisation.

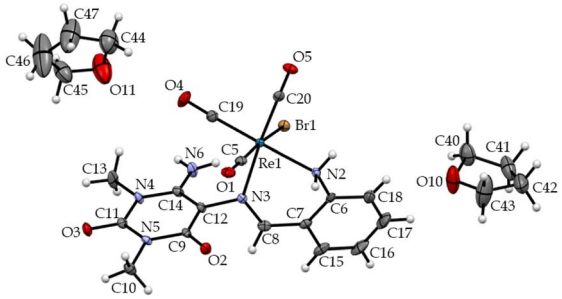

Fig. 3 Crystal structure of **2** with two tetrahydrofuran molecules of recrystallisation.

molecules of recrystallisation allow both independent crystallographic molecules to pack in columns aligned with the [*a*] and [*b*] axes, while molecules B of **1** run parallel with the [*c*] axis, see Fig. S19. More specifically, the hydrogen bonding interactions observed in **1** includes: Cl1···H71 [2.64(3) Å], Cl1···H80 [2.42(5) Å], Cl2···H72 [2.36(5) Å], Cl2···H82 [2.86(4) Å], O9···H70 [2.12(4) Å], O5···H83 [2.15(5) Å], O10···H81 [2.05(4) Å], O11···H82 [2.33(4) Å] and O11···H73 [2.06(4) Å]. Indicatively, neighbouring molecules of **2** are interlinked through classical hydrogen-bonding contacts which are further supported through contacts with the adjacent solvent molecules of recrystallization: O2···H63 [2.24(4) Å], O1···H63 [2.29(4) Å], O5···H62 [2.86(4) Å] and O3···H61 [2.00(4) Å] while intramolecular interaction occurs between the bromo co-ligand and one of the amino hydrogens [Br1···H60 = 2.71(4) Å], see Fig. S20. Consequently, the molecules of **2** stacks are perpendicular to the [*a*]-axis but parallel to the [*b*] and [*c*]-axes.

The main stabilising factors of the crystal lattice for **3** also constitute intramolecular bonding [Br1···H7 = 2.6437 Å for **3**], see Fig. 4. The aforementioned interactions facilitate the molecules of **3** to pack in columns parallel to the [*b*]-axis, see Fig. S21. The variable degree of flexibility along the aliphatic imino functionalities induces different dihedral angles. In particular, the individual uracil and phenyl groups of **2** lie at 68.72° and 38.56° out of the defined C19C20N2N3 equatorial plane. The respective quinoline and uracil planes cut the defined equatorial N1N2C1C2 plane of **3** by 9.22° and the 64.07°. Crystallographic independence of the two molecules for

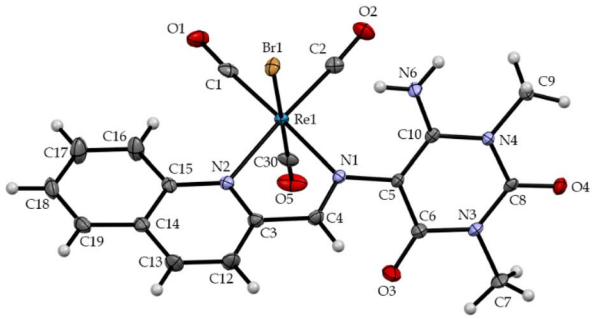

Fig. 4 X-ray structure of **3**.

1 is further emphasised by their different dihedral angles between corresponding uracil rings and basal planes: N9O15C1C2 at 8.29° for molecule **B** and N5O14C11C13 at 18.19° for molecule **A**.

The metal centres of **1**–**3** are in the centres of their corresponding distorted octahedra, which are largely induced by their constrained bite angles: O15–Re1–N9 = 76.94(9)° and O14–Re2–N5 = 76.88(9)° for **1**, N3–Re1–N2 = 83.2(1)° for **2** and 74.95(6)° for **3**, see Tables S2–S4. The latter geometrical parameters lead to non-linearity in the bond angles [C2–Re1–N9 = 172.6(1)°, C31–Re1–O15 = 171.8(1)°, C12–Re2–O14 = 175.6(1)° and N5–Re2–C11 = 172.7(1)° for **1**, N2–Re1–C19 = 177.0(1)°, C20–Re1–N3 = 175.3(1)° for **2** and C1–Re1–N2 = 176.87(8)°, N2–Re1–C2 = 172.34(8)° for **3**] making up the defined equatorial planes of C2C31N9O15 and C12C11N5O4 for **1**, C19C20N2N3 for **2** and C1C2N1N2 for **3**. With the exception of **3** with a Br1–Re1–C30 bond angle of 178.31(7)°, the assigned individual axial planes [C11–Re1–C12 = 173.0(5)°, Cl3–Re2–Cl1 = 174.7(1)° for **1** and C5–Re1–Br1 = 173.5(1)° for **2**] of the remaining Complex considerably deviates from the 180° ideal octahedral angle which could be largely ascribed to the intermolecular interactions occurring with the halide co-ligands.

Rhenium-to-carbonyl bond distances of **2** and **3** are comparable to those found within other *facial* tricarbonylrhenium complexes having Re–C bonds in the ranges of 1.892(7)–1.954(7) Å.[8,14,16] Aside from molecule **A** of **1**, where the equatorial and axial Re–C bonds are identical, the Re–C bonds of the other metal Complex differs, which is attributed to the influence of the *trans*-positioned donor atoms imposed on the corresponding organometallic bonds. In **1**, Re–$O_{ketonic}$ bonds [Re(1)–O(15) = 2.181(2) Å, and Re(2)–O(14) = 2.1660(19) Å] are relatively similar to those found within other tricarbonyl rhenium(I) complexes: *fac*-[$Re(CO)_3Cl$(DANTU)] (DANTU = 6-amino-1,3-dimethyl-5-nitroso-2-thiouracil), *fac*-[$Re(CO)_3(H_2O)$ ($VIOH_{-1}$)] ($VIOH_{-1}$ = violuric acid) and *fac*-[$Re(CO)_3(H_2O)$($DVIOH_{-1}$)] ($DVIOH_{-}1$ = dimethyl violuric acid) with bond lengths of 2.166(4) Å, 2.159(6) Å and 2.141(4) Å, respectively.[11] Furthermore, Re–N bonds of **1** [2.207(3) Å and 2.215(3) Å] are longer than those of the other metal complexes, which can be simply ascribed to the variable hybridizations of amino nitrogen in **1** oppose to the imino nitrogen atoms in the **2** and **3** [2.187(3) Å, 2.1694(17) Å and 2.1852(18) Å].

A noticeable difference is observed within the Re–Cl bond distances [Re1–Cl2 = 2.4775(7) Å and Re2–Cl1 = 2.4945(7) Å] of **1**, which is tentatively ascribed to different inter- and intramolecular interactions experienced by molecules **A** and **B**. However, the aforementioned coordination bonds are still close to the upper and lower limits of analogous bonds [*viz*. Re–Cl = 2.4741(8)–2.499(1) Å] of other rhenium(I) complexes.[8,16] The larger atomic radius of the bromide co-ligands affords longer metal coordinative bonds [Re–Br = 2.6221(4) Å for **2** and 2.6064(2) Å for **4**] than the rhenium-to-chloride bonds[17,18]

Interestingly, the ketonic bond in the solid-state structure of uncoordinated urda has a bond distance of 1.237(2) Å, which is lengthening to 1.273(4) Å [C17–O15 in molecule **A**] and 1.269(4) Å [C4–O14 in molecule **B**] upon coordination to the respective metal centres, while the uncoordinated C=O bonds of **1** (1.224(3) Å [C18–O9 in molecule **A**] and 1.227(5) Å [C7–O5 in molecule **B**]) are nearly the same as found within the crystal structure of free urda.[19] As expected for imino aliphatic bonds with a bond order of 2 [1.291(4) Å for **2** and 1.288(3) Å for **3**], their bond lengths are shorter than those of the uracil [1.381(5) Å and 1.383(3) Å for **1**, 1.377(4) Å for **2** and 1.401(3) Å for **3**].[8]

In vitro anti-cancer studies

Cytotoxicity of metal complexes. Complex **1** was the most potent in its cytotoxicity towards the HeLa cervical cancer cell line, while being non-toxic to both the HCC70 TNBC and MCF12A non-cancerous breast epithelial cell lines, as shown in Table 1. Interestingly, this means that complex **1** shows selective activities between the two cancer cell lines, cervical *versus* breast cancer, and between a cervical cancer cell line and a non-cancerous cell line (selectivity index = 73). On the other hand, complex **2** displayed a high degree of cytotoxicity in both cancer cell lines. In particular, complex **2** displayed an IC_{50} value of 5 μM (5.233 ± 1.0280 μM) in the HCC70 cell line and an IC_{50} value of 10 μM (9.862 ± 1.0852 μM) in the HeLa cell line. However, the metal compound was also highly toxic to the MCF12A cells, displaying an IC_{50} value of 8 μM (7.817 ± 1.1261 μM), indicating a lack of selectivity for cancer cells over non-cancerous cells.

Complex **3** was less potent to the HeLa cells, with an IC_{50} value of 101 μM (100.7 ± 1.1427), while it displayed moderate cytotoxicity against the HCC70 cells, with an IC_{50} value of 13 μM (12.61 ± 1.1083), again reflecting a difference in toxicity between breast and cervical cancer cell lines, however displaying an inverse trend to that displayed by complex **1**. Complex **3** was also relatively toxic to MCF12A cells, displaying an IC_{50} of 15 μM (14.64 ± 1.1859) in this cell line. Complex **2** was selected as the focus for further mechanistic analysis based on its high cytotoxicity overall.

Comparatively, the chemotherapeutic drug, paclitaxel, was more toxic to all three cell lines and produced IC_{50} values in the nanomolar range. In particular, IC_{50} values of 54 nM (54.34 ± 1.0565 nM) and 67 nM (66.98 ± 1.0174 nM) were obtained in HCC70 and HeLa cells, respectively.[20,21] The organotherapeutic cancer drug, paclitaxel, can, however, be classified as non-selective as indicated by the similar IC_{50} value of 88 nM (87.86 ± 1.0819 nM) obtained in the non-tumorigenic MCF12A cell line. Despite this lack of selectivity, paclitaxel is currently used in the clinic to treat various cancers.[22]

Ability of complex 2 to inhibit long-term survival. A clonogenic assay was carried out to assess the effect of complex **2** on the long-term survival of HCC70 TNBC cells *in vitro*. This assay is used to assess the ability of individual cells to establish colonies as a measure of unlimited cell division over an extended culture period following an initial 48 h exposure to a compound (Franket *et al.*) and was included as further support of the cytotoxicity of complex **2**.[23] A dose-dependent and statistically significant decrease in the number of colonies and absorbance of the crystal violet stain at 595 nm following solubilization was observed after treatment with 5, 25, or 125 μM of the complex relative to the corresponding DMSO vehicle control (see Fig. 5). These findings indicate a direct inhibition of cell division according to cell number, and not metabolic activity, as assessed by the resazurin and other standard cytotoxicity assays.

DNA binding studies

Assessment of the ability of complex 2 to bind to human and bovine genomic DNA by intercalation. Prior to exploring the affinities of the metal complex towards DNA, its stability was assessed in ultrapure water and aqueous PBS buffer using UV-Vis spectrophotometry. Sequential additions of ultrapure water aliquots to standardized solutions of **1–3** revealed that no observable electronic spectral changes occurred, which indicates that the structural integrity of each metal complex in solution was retained. Similarly, the high stability of **2** in deuterated dimethylsulphoxide was corroborated by its ^{1}H NMR spectral data, which showed no distinctive changes over several days.

Table 1 IC_{50} values of **1–3** and paclitaxel against cancer and non-cancerous cell lines

Complex	HCC70/μM (IC_{50} and SD) R^2	HeLa/μM (IC_{50} and SD) R^2	MCF12A/μM (IC_{50} and SD) R^2
1	IC50 > 400	3.174 ± 1.0727	230.7 ± 1.4181
	* NT	0.9859	0.9564
2	5.233 ± 1.0280	9.862 ± 1.0852	7.817 ± 1.1261
	0.9986	0.9953	0.9986
3	12.61 ± 1.1083	100.7 ± 1.1427	14.64 ± 1.1859
	0.9839	0.9934	0.9877
Paclitaxel	54.34 ± 1.0565 nM	66.98 ± 1.0174 nM	87.86 ± 1.0819 nM
	0.9706	0.9968	0.9351

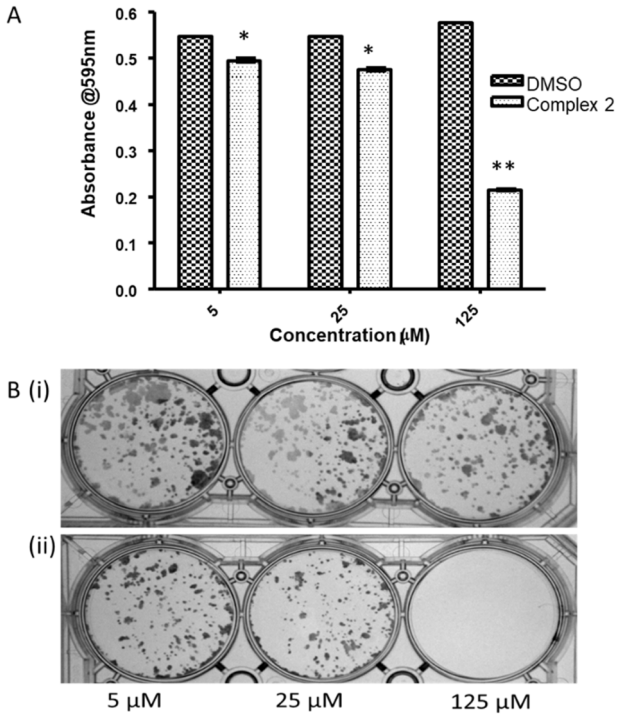

Fig. 5 Clonogenic assay to determine the effect of complex **2** on long-term survival of TNBC cells. (A) Graphical representation of the solubilized crystal violet staining of HCC1806 breast cancer cells treated with complex **2** in comparison to that of the DMSO vehicle control as a measure of the number of total cells present after 10 days of incubation. (B) Representative images of the crystal violet-stained HCC1806 colonies after 10 days prior to solubilization. (i) DMSO treatments corresponding to (ii) the various treatment concentrations of complex **2**. Data is expressed as mean ± standard deviation in triplicate ($n = 3$) with $^{*}p < 0.05$ and $^{**}p < 0.01$.

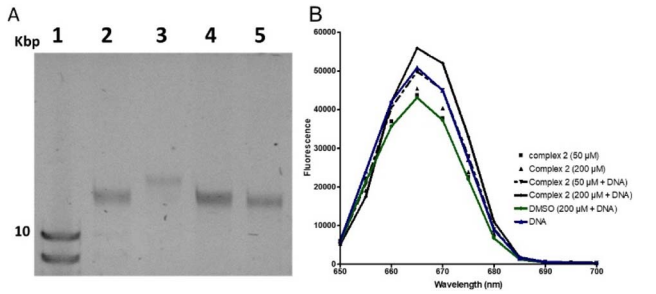

Fig. 6 Assessment of the ability of complex **2** to intercalate into human genomic and calf thymus DNA (**A**) Ethidium bromide competition assay. Ethidium bromide-stained 0.6% (w v^{-1}) agarose gel containing human genomic DNA incubated with DMSO, cisplatin, or complex **2**. Lane 1: Quick Load Purple 1 Kb Plus DNA Ladder (N0550S); Lane 2: DMSO [0.2% (v/v)] control; Lane 3: cisplatin (200 μM); Lane 4: complex **2** (50 μM); Lane 5: complex **2** (200 μM). (**B**) Methylene blue competition assay. Fluorescence emission spectra for methylene blue incubated with calf thymus DNA with or without the addition of complex **2**. The experiment was performed in triplicate, and the standard deviation ($n = 3$) is displayed as error bars.

The ability of complex **2** to bind to genomic DNA extracted from HCC70 TNBC cells was assessed by agarose gel electrophoresis and ethidium bromide (EtBr) competition. EtBr is a DNA intercalating fluorescent dye (Sigmon and Larcom, 1996) and thus a decrease in band intensity indicates that a compound is able to bind to the DNA and displace EtBr.[24] This is observed for the cisplatin positive control, a known DNA intercalator, but is not observed for complex **2** at either 50 or 200 μM, in comparison to the DMSO control (see Fig. 6A).[25]

Next, a more sensitive methylene blue assay was performed to assess the intercalation ability of complex **2** spectroscopically. Methylene blue produces a fluorescent peak between 660 and 680 nm; however, this is quenched when the dye is bound to DNA.[26,27] A competitive intercalator would thus result in increased methylene blue fluorescence, and this is indeed observed for complex **2** at the higher concentration of 200 μM, in relation to the DNA alone, compounds alone, or DNA and DMSO controls (see Fig. 6B).

ctDNA UV-Vis spectrophotometric titration and molecular docking studies of 2. Generally, the steric demands of octahedral organometallic rhenium(I) complexes induce DNA groove binding modes, which result in hyperchromic effects of their ligand-based electronic transitions.[14,28,29] However, rhenium compounds with a high degree of planarity of their aromatic chromophores can facilitate intercalation between the DNA base pairs, which typically manifest as progressive increases in the absorbance values of π–π* intra-ligand electronic transitions (*i.e.*, hypochromism) accompanied by gradual red-shifting (*i.e.*, bathochromism).[30,31] The presence of isosbestic points in UV-Vis spectral profiles of the organic or inorganic compounds during CT-DNA titrations has been associated with a single or various DNA binding forms.[30,32,33]

The UV-Vis spectral profile of **2** illustrates hyperchromism of its pi–pi* intra-ligand electronic transition at 363 nm upon sequential additions of CT-DNA, see Fig. S22. This spectral trend is synonymous with DNA groove-binding, which is supported by the fact that the intrinsic DNA binding constant of **2** (3.0×10^4 M^{-1}) which is below those of DNA intercalating octahedral d-block metal complexes with K_b values > 10^6 M^{-1}.[34,35] However, a diffused isosbestic point at 412 nm is indicative of different DNA-metal complex adducts forming during the respective titrimetric experiments. Therefore, it can be hypothesised that metal complex **2** is classified as a tandem DNA intercalator and groove-binder.

The DNA binding experimental studies were corroborated by the *in silico* studies using the optimised conformer of **2** and DNA structural conformers produced from different DNA crystal structures. The lowest energy metal complex-DNA adducts revealed that **2** can computationally exhibit both DNA groove-binding capability and intercalation modes simultaneously. Energetically, the DNA intercalating metal complex into DNA structure generates a lower binding energy of −12.59 kcal mol^{-1} compared to the binding energy of −6.62 kcal mol^{-1} when the optimised conformer of **2** occupies the DNA major groove, see Fig. S23 and S24. Consequently, the computational data affirms the experimental trends found within the competitive DNA binding assays and UV-Vis spectrophotometric titrations.

Assessment of the ability of complex 2 to induce DNA damage and interfere with topoisomerase function. In order to assess the ability of metal complex **2** to damage nuclear DNA in TNBC cells, a comet assay was performed on intact HCC70 cells. This assay detects single and double-strand breaks as well as alkali-labile lesions as a "comet" of diffuse stain extending from the nucleus upon AGE.[36] In this assay, metal complex **2** treatments at either 10 or 20 μM (consistent with the IC_{50} values obtained during cytotoxicity screening) for 2 hours was unable to cause significant DNA damage according to olive moment, which is the product of the percentage of the total DNA in the tail (tail percentage) and the distance between the head and tail of the cells (tail length) [tail DNA% × (length of tail – length of head)]. This was determined for a minimum of 100 individual comets per treatment (see Fig. 7A). Next, the effect on topoisomerase (Topo) activity was assessed according to whether complex **2** was able to interfere with the ability of Topo I to relax supercoiled DNA. Topoisomerases are validated drug targets for cancer and topoisomerase inhibition has been linked to DNA damage induction.[37] This is due to the inhibition of the enzyme's function, namely, to cause transient single or double-stranded breaks during replication and transcription to relieve torsional strain on the DNA molecule. When this is inhibited, the DNA can be damaged during replication and transcription by excessive torsional strain (Xu and Her 2011).[38] As observed in Fig. 7B, addition of Topo I to supercoiled plasmid DNA, causes nicking and relaxation of the plasmid such that the DNA band moves to a higher position on the agarose gel (Fig. 7B lane 2 *vs.* lane 4). This indicates that the Topo I was active. The addition of a Topo inhibitor should result in a downwards shift back towards the supercoiled confirmation; however, this is not observed for complex **2** (Lanes 5 and 6 of Fig. 7B), suggesting no significant inhibition of Topo I by the complex. This suggests a different mechanism of action of this rhenium complex, as compared to complexes of ruthenium, which are known to inhibit topoisomerase function.[39,40]

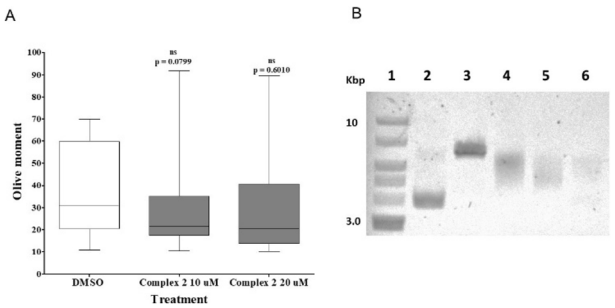

Fig. 7 Assessment of potential DNA damage induction and topoisomerase inhibition by complex **2** (A) results of the alkaline comet assay carried out on HCC70 cells. DNA damage analysis was performed using the OpenComet PlugIn with ImageJ software and quantified according to olive moment. Statistical analysis was performed using the Mann–Whitney t-test, $n > 100$, ns – not significant. (B) Topoisomerase I inhibition assay analysed on a 0.6% (w v^{-1}) agarose gel with ethidium bromide secondary staining. Lane 1: DNA ladder (Biolabs NO55OS 1 kb); Lane 2: Supercoiled pcDNA; Lane 3: linearised pcDNA following HindIII digestion, Lane 4: Topo I and pcDNA plasmid; Lane 5: complex **2** (50 μM) with Topo I and pcDNA plasmid; Lane 6: complex **2** (200 μM) with Topo I and pcDNA plasmid.

Conclusions

Novel rhenium(I) complexes containing uracil derivatives were synthesised and characterised by various physicochemical techniques. Their solid-state structures exhibited distorted octahedral geometries, which are largely caused by their constrained five or six-membered chelate rings. The metal complexes **1–3** displayed varying cytotoxicity and selectivity when tested against HCC70 breast cancer, HeLa cervical cancer, and MCF12A non-tumorigenic breast epithelial cell lines, with metal complex **2** showing the greatest cytotoxicity, in the low micromolar range, against all three cell lines. In addition, metal complex **2** could tandemly bind to DNA through intercalation and groove-binding, but did not cause DNA damage when assessed in a comet assay and did not interfere with topoisomerase I activity in relaxing supercoiled DNA, compared to ruthenium compounds.

Author contributions

Shabaaz Abdullah (SA): writing – original draft preparation, methodology, formal analysis, investigation, data curation, visualisation. Candice Davison (CA): methodology, investigation. Andile Kathi: writing – review & editing, resources. Christie Jane Smit (CJS): writing – original draft preparation, methodology, formal analysis, investigation, data curation, visualisation, Phiwokuhle Mbatha (PM): formal analysis, investigation, data curation, visualisation, Jo-Anne de la Mare (JDLM): funding acquisition, conceptualisation, writing – review & editing, co-funding and resources, supervision of CJS, co-host of CA. Irvin Noel Booysen: funding acquisition, conceptualisation, writing – review & editing, methodology, co-funding and resources, supervision of SA.

Conflicts of interest

There are no conflicts to declare.

Data availability

Data is available from the corresponding authors upon reasonable request.

CCDC 2091662, 2091664 and 2091665 contain the supplementary crystallographic data for this paper.[41a–c]

Supplementary information is available. See DOI: https://doi.org/10.1039/d5ra05387k.

Acknowledgements

This work was supported by the Nuclear Technologies in Medicine and the Biosciences Initiative (NTeMBI). NTeMBI is a national technology platform developed and managed by the South African Nuclear Energy Corporation (Necsa) and funded by the Technology Innovation Agency (TIA). The authors would

like to thank the University of KwaZulu-Natal for the use of their facilities and equipment. The anti-cancer studies were supported by a Thuthuka NRF (Research Grant No. 94020 and 190403426633) and Rhodes University. The views expressed are those of the authors and should not be attributed to NECSA, NTeMBI, Rhodes University, or the University of KwaZulu-Natal. The Centre for High Performance Computing (CHPC), South Africa, for providing computational resources to this research project.

References

1 J. Lecina, Ò. Palacios, S. Atrian, M. Capdevila and J. Suades, *JBIC, J. Biol. Inorg. Chem.*, 2015, **20**, 465–474.
2 A. Shegani, C. Triantis, B. A. Nock, T. Maina, C. Kiritsis, V. Psycharis, C. Raptopoulou, I. Pirmettis, F. Tisato and M. S. Papadopoulos, *Inorg. Chem.*, 2017, **56**, 8175–8186.
3 G. Makris, L. L. Radford, M. Kuchuk, F. Gallazzi, S. S. Jurisson, C. J. Smith and H. M. Hennkens, *Bioconjug. Chem.*, 2018, **29**, 4040–4049.
4 M. A. Klenner, B. H. Fraser, V. Moon, B. J. Evans, M. Massi and G. Pascali, *Eur. J. Inorg. Chem.*, 2020, **2020**, 3554–3564.
5 M. D. Bartholomä, A. R. Vortherms, S. Hillier, J. Joyal, J. Babich, R. P. Doyle and J. Zubieta, *Dalton Trans.*, 2011, **40**, 6216–6225.
6 M. T. Gabr and F. C. Pigge, *Dalton Trans.*, 2017, **46**, 15040–15047.
7 P. Mayer, E. Hosten, T. Gerber and I. Booysen, *J. Iran. Chem. Soc.*, 2010, **7**, 775–780.
8 K. Potgieter, P. Mayer, T. Gerber, N. Yumata, E. Hosten, I. Booysen, R. Betz, M. Ismail and B. van Brecht, *Polyhedron*, 2013, **49**, 67–73.
9 D. Ramesh, B. G. Vijayakumar and T. Kannan, *Eur. J. Med. Chem.*, 2020, 112801.
10 C. Davison, S. Abdullah, C. J. Smit, P. Dlamini, I. N. Booysen and J.-A. d. l. Mare, *Chem.-Biol. Interact.*, 2025, **406**, 111351.
11 N. A. Illán-Cabeza, A. R. García-García and M. N. Moreno-Carretero, *Inorg. Chim. Acta*, 2011, **366**, 262–267.
12 I. Machado, S. Fernández, L. Becco, B. Garat, J. S. Gancheff, A. Rey and D. Gambino, *J. Coord. Chem.*, 2014, **67**, 1835–1850.
13 I. Ebinumoliseh, I. N. Booysen, M. P. Akerman and B. Xulu, *J. Mol. Struct.*, 2016, **1123**, 8–13.
14 M. B. Ismail, I. N. Booysen, E. Hosten and M. P. Akerman, *J. Organomet. Chem.*, 2017, **833**, 1–9.
15 E. Kottelat, F. Lucarini, A. Crochet, A. Ruggi and F. Zobi, *Eur. J. Inorg. Chem.*, 2019, **2019**, 3758–3768.
16 N. A. Illán-Cabeza, A. R. García-García, M. N. Moreno-Carretero, J. M. Martínez-Martos and M. J. Ramírez-Expósito, *J. Inorg. Biochem.*, 2005, **99**, 1637–1645.
17 P. A. Abramov, A. A. Dmitriev, K. V. Kholin, N. P. Gritsan, M. K. Kadirov, A. L. Gushchin and M. N. Sokolov, *Electrochim. Acta*, 2018, **270**, 526–534.
18 B. R. Schrage, R. S. Herrick and C. J. Ziegler, *J. Organomet. Chem.*, 2019, **880**, 170–174.
19 F. Hueso-Ureña, M. N. Moreno-Carretero, J. N. Low and A. G. Masterton, *J. Mol. Struct.*, 1997, **435**, 133–141.
20 Y. A. Larasati, D. P. Putri, R. Y. Utomo, A. Hermawan and E. Meiyanto, *J. Appl. Pharmaceut. Sci.*, 2014, **4**, 14–19.
21 A. M. Heijink, M. Everts, M. E. Honeywell, R. Richards, Y. P. Kok, E. G. de Vries, M. J. Lee and M. A. van Vugt, *Cell Rep.*, 2019, **28**, 2345–2357.
22 Y.-H. Yang, J.-W. Mao and X.-L. Tan, *Chin. J. Nat. Med.*, 2020, **18**, 890–897.
23 N. A. P. Franken, H. M. Rodermond, J. Stap, J. Haveman and C. van Bree, *Nat. Protoc.*, 2006, **1**, 2315–2319.
24 J. Sigmon and L. L. Larcom, *Electrophoresis*, 1996, **17**, 1524–1527.
25 H. Baruah, C. G. Barry and U. Bierbach, *Curr. Top. Med. Chem.*, 2004, **4**, 1537–1549.
26 G. A. Shahinyan, A. Y. Amirbekyan and S. A. Markarian, *Spectrochim. Acta, Part A*, 2019, **217**, 170–175.
27 P. O. Vardevanyan, A. P. Antonyan, M. A. Parsadanyan, M. A. Shahinyan and L. A. Hambardzumyan, *J. Appl. Spectrosc.*, 2013, **80**, 595–599.
28 M. B. Ismail, I. N. Booysen and M. P. Akerman, *Inorg. Chim. Acta*, 2018, **477**, 257–269.
29 M. B. Ismail, I. N. Booysen, M. P. Akerman and C. Grimmer, *J. Organomet. Chem.*, 2017, **833**, 18–27.
30 C.-C. Pagoni, V.-S. Xylouri, G. C. Kaiafas, M. Lazou, G. Bompola, E. Tsoukas, L. C. Papadopoulou, G. Psomas and D. Papagiannopoulou, *JBIC, J. Biol. Inorg. Chem.*, 2019, **24**, 609–619.
31 T. Mapapiro, C. Davison, A. Mambanda, J.-A. de la Mare and I. N. Booysen, *ChemistrySelect*, 2024, **9**, e202400493.
32 P. Vardevanyan, V. Élbakyan, M. Shahinyan, M. Minasyants, M. Parsadanyan and N. Sahakyan, *J. Appl. Spectrosc.*, 2015, **81**, 1060–1063.
33 K. Jomová, L. Hudecova, P. Lauro, M. Simunkova, S. H. Alwasel, I. M. Alhazza and M. Valko, *Molecules*, 2019, **24**, 4335.
34 B. J. Pages, D. L. Ang, E. P. Wright and J. R. Aldrich-Wright, *Dalton Trans.*, 2015, **44**, 3505–3526.
35 M. B. Ismail, I. N. Booysen and M. P. Akerman, *Inorg. Chem. Commun.*, 2017, **78**, 78–81.
36 X. Pu, Z. Wang and J. E. Klaunig, *Curr. Protoc. Toxicol.*, 2015, **65**, 3.12.11–13.12.11.
37 E. Schneider, Y.-H. Hsiang and L. F. Liu, in *Advances in Pharmacology*, ed. T. August, M. W. Anders, F. Murad and A. Nies, Academic Press, 1990, vol. 21, pp. 149–183.
38 Y. Xu and C. Her, *Biomolecules*, 2015, **5**, 1652–1670.
39 C. C. Konkankit, S. C. Marker, K. M. Knopf and J. J. Wilson, *Dalton Trans.*, 2018, **47**, 9934–9974.
40 S. Maikoo, C. Davison, J.-A. de la Mare and I. N. Booysen, *Polyhedron*, 2023, **245**, 116640.
41 (*a*) S. Abdullah, C. Davison, C. Smit, P. Mbatha, J. Mare, I. Booysen, CCDC 2091662: Experimental Crystal Structure Determination, 2025, DOI: **10.5517/ccdc.csd.cc286jz0**; (*b*) S. Abdullah, C. Davison, C. Smit, P. Mbatha, J. Mare, I. Booysen, CCDC 2091664: Experimental Crystal Structure Determination, 2025, DOI: **10.5517/ccdc.csd.cc286k13**; (*c*) S. Abdullah, C. Davison, C. Smit, P. Mbatha, J. Mare, I. Booysen, CCDC 2091665: Experimental Crystal Structure Determination, 2025, DOI: **10.5517/ccdc.csd.cc286k24**.